

# Automatic Segmentation of Echocardiographic Sequences by Active Appearance Motion Models

Johan G. Bosch\*, Steven C. Mitchell, Boudewijn P. F. Lelieveldt, Francisca Nijland, Otto Kamp, Milan Sonka, *Fellow, IEEE*, and Johan H. C. Reiber, *Senior Member, IEEE*

**Abstract**—A novel extension of active appearance models (AAMs) for automated border detection in echocardiographic image sequences is reported. The active appearance motion model (AAMM) technique allows fully automated robust and time-continuous delineation of left ventricular (LV) endocardial contours over the full heart cycle with good results. Nonlinear intensity normalization was developed and employed to accommodate ultrasound-specific intensity distributions. The method was trained and tested on 16-frame phase-normalized transthoracic four-chamber sequences of 129 unselected infarct patients, split randomly into a training set ( $n = 65$ ) and a test set ( $n = 64$ ). Borders were compared to expert drawn endocardial contours. On the test set, fully automated AAMM performed well in 97% of the cases (average distance between manual and automatic landmark points was 3.3 mm, comparable to human interobserver variabilities). The ultrasound-specific intensity normalization proved to be of great value for good results in echocardiograms. The AAMM was significantly more accurate than an equivalent set of two-dimensional AAMs.

**Index Terms**—Active appearance models (AAMs), echocardiography, model-driven segmentation, time sequences.

## I. INTRODUCTION

ULTRASOUND imaging allows direct visualization of the heart in motion. Image sequences of standard cross-sectional views through the heart provide insight in the functional performance of the different segments of the left ventricular (LV) wall. It is widely recognized that quantitative analysis of echocardiograms is preferable over qualitative interpretation, in particular for wall motion and volume estimation. However, manual measurements are tedious and time consuming, require expert knowledge, and suffer from considerable inter- and intraobserver variability. Semiautomated methods are either too unreliable or require too much interaction, especially

when many sequences need to be analyzed, e.g., for stress echo studies. Therefore, robust and highly automated border detection of endocardium and other structures is desired.

### A. Echocardiographic Image Segmentation

Ultrasound suffers from several specific drawbacks, which impede both human interpretation and automated analysis.

- 1) There is no simple relation between pixel intensity and any physical property of the tissue visualized, in contrast to, e.g., the Lambert–Beer law for X-ray. Ultrasound images are formed as a combination of interference patterns (speckle) and reflections at tissue transitions. Different tissues are mostly not distinguishable by their intensity values or texture.
- 2) Ultrasonic image information is highly anisotropic and position dependent, since reflection intensity, spatial resolution, and signal-to-noise (S/N) ratio depend on the depth and the angle of incidence of the ultrasound beam, as well as of user-controlled depth gain settings.
- 3) Many imaging artifacts occur, resulting in local loss of anatomical information: significant amounts of noise, dropouts (for structures parallel to the ultrasound beam), shadowing (behind acoustically dense structures), side-lobes, reverberations, and limited echo windows. Still-frame images, therefore, often only contain partial information.

For these reasons, automated segmentation of echocardiographic image sequences has proven to be a challenging task. Many approaches to segmentation of the endocardium in echocardiographic data have been proposed (for overviews, see [1] and [2]) based on, among others, integrated backscatter RF processing [3], arc filters [4], fuzzy neural nets [5], dynamic programming [1], [6], [7], simulated annealing [8], self-organizing maps [9], snakes/active contours [10], [11], and active shape models (ASMs) [12], [13]. Though partially successful, three major problems are associated with many of the existing echocardiographic contour detection strategies.

- 1) The current methods typically do not include information about the allowable range of shape and appearance variations of the segmented objects. Ultrasonic image information is often ill-defined or incomplete. Therefore, extensive model knowledge about the characteristic organ shape and appearance, its anatomical and pathological shape variations and spatial organ embedding should form an integral part of a robust segmentation approach.
- 2) Most existing methods use implicit, global, and oversimplified models for the contour location (e.g., strongest edges).

Manuscript received August 1, 2001; revised July 25, 2002. This work was supported by the Technology Foundation, The Netherlands, under Project LGN4349 and in part by the Leiden University Medical Center by the realization of the honorary Boerhaave Professorate of M. Sonka, Spring 1999. The Associate Editor responsible for coordinating the review of this paper and recommending its publication was A. Manduca. Asterisk indicates corresponding author.

\*J. G. Bosch is with the Division of Image Processing (LKEB), Department of Radiology, Leiden University Medical Center, P.O. Box 9600, 2300 RC Leiden, The Netherlands (e-mail: j.g.bosch@lumc.nl).

S. C. Mitchell and M. Sonka are with the Department of Electrical and Computer Engineering, University of Iowa, Iowa City, IA 52242 USA.

B. P. F. Lelieveldt and J. H. C. Reiber are with the Division of Image Processing, Department of Radiology, Leiden University Medical Center, 2300 RC Leiden, The Netherlands.

F. Nijland and O. Kamp are with the Department of Cardiology, Vrije Universiteit Medical Center, 1081 HV Amsterdam, The Netherlands.

Digital Object Identifier 10.1109/TMI.2002.806427

The location of strong local image features, however, does not always correspond to the desired contour as drawn by an expert human observer. In particular, the papillary muscles and trabeculations pose a problem, as well as the mentioned anisotropy and artifacts. Therefore, the exact location of the contour cannot always be determined from the strongest image evidence, but should be modeled or learned from examples provided by expert observers. Moreover, contour characteristics vary for different parts of the local (and yet unknown) anatomy.

- 3) Many automated techniques perform a static segmentation on single two-dimensional (2-D) frames or use rudimentary continuity constraints and, therefore, often produce segmentation results that are inconsistent with the dynamics of the cardiac cycle. An expert observer, however, utilizes knowledge about cardiac contraction dynamics and temporal coherence of structures and texture to resolve ambiguities and to determine the exact LV boundary location, mostly after reviewing the image data in a cine loop.

Recently, several methods have been reported that try to deal with the third problem in time sequences of either 2-D or three-dimensional (3-D) echocardiograms. Montagnat *et al.* [14] report a time-continuous segmentation in 3-D time sequences based on a two-simplex mesh deformable surface and a feature detection by a cylindrical Deriche gradient filter. Time continuity is enforced by propagating the found surface as a model to following time frames. Results are shown for one clinical example. Angelini *et al.* [15] mainly aim at feature enhancement and speckle suppression in four-dimensional (4-D) echos using so-called 4-D brushlets, which are wavelet-like decompositions of the spatial frequency domain. A standard 2-D balloon consecutively performs segmentation in short-axis cross sections. Promising results on six patients are reported, but significant manual interaction and very time-consuming processing is required. Jacob *et al.* [16] describe a statistical shape model trained from example contours by principal component analysis, combined with a Kalman filter approach for prediction of dynamic shape changes and a feature detection based on temporal smoothing, integrated backscatter calculation, and one-dimensional log-Gabor filters. The practical value of these approaches remains uncertain due to the limited testing on clinical image data.

### B. Active Appearance Models (AAMs)

AAM matching is a highly promising segmentation technique that may provide new solutions to these problems. The AAM technique was recently introduced by Cootes *et al.* [17], [18] and forms an extension of the widely applied ASMs [13] from which it inherited the shape-modeling approach. An AAM describes both image appearance and object shape over a set of examples as a combined statistical shape–appearance model. AAMs can be applied to image segmentation through analysis-by-synthesis, by minimizing the difference between a model-generated synthetic image patch and a real image using statistically plausible parameter adjustments. We have shown earlier that AAMs are highly robust in the segmentation of routinely acquired single-phase single-slice cardiac magnetic

resonance (MR) images [19] and end-diastolic echocardiograms [20], because they exploit *a priori* knowledge of the cardiac shape, image appearance, and observer preference in a generic way. AAMs model the complete object appearance, including typical local position-dependent artifacts such as lateral wall dropouts. Since ultrasound images are generally acquired in standardized cross sections, typical problems occur in the same parts of the anatomy in most of these images. A technique like AAM can model such typical local effects. Moreover, effects of high spatial frequency and a more random nature such as speckle and noise are suppressed by the spatial averaging and principal component analysis (PCA). Averaging the images retrieves the reproducible information in a generalized form. Furthermore, since AAMs are trained from expert-segmented examples, they mimic the expert’s segmentation decisions in cases of typical artifacts. The AAM will also cover the shape and appearance variability in the example set. Provided that the example set is representative of the variability in the population and the distribution can be approximated by a high-dimensional Gaussian ellipsoid, an AAM can generate any statistically plausible intermediates [18]. If the distribution is disjunct or very skewed, the model may generate implausible intermediates or may fail to cover the full range of variability. In practice, it was not a problem in our experiments.

These properties of the AAM cover most of the typical problems of ultrasound segmentation as listed above. However, the sequential application of 2-D AAMs to a time sequence does not guarantee a time-continuous segmentation result because it does not exploit temporal coherency in the data. Moreover, to apply 2-D AAMs to segmentation of a full cardiac cycle, multiple models may be required for different phases of the cardiac cycle (rather than an overly generalized model for all phases).

In this paper, a novel active appearance motion model (AAMM) for normalized time sequences of 2-D images is presented that models the shape and appearance of the heart in combination with the dynamics of the cardiac cycle. This way, the proven strong points of AAMs (robustness, ability to capture observer preference) can be augmented with temporal consistency over an image sequence. Cootes’ 2-D AAM framework was extended to time sequences by considering a whole image sequence as a single shape/intensity sample. As an important contribution to the successful application of AAMMs for echocardiographic image segmentation, a specific nonlinear intensity normalization is introduced.

## II. METHODS

### A. AAMs

The AAM approach has been extensively described [17]–[19]. A concise overview of the general AAM approach is given here to clarify the place of the described extensions. Generating an AAM requires three stages.

- 1) Generating a statistical model describing shape and appearance over a set of normalized and aligned hand-annotated examples. From a small set of model parameters, an appearance model can generate synthetic images closely resembling the original examples *and* statistically plausible intermediates.

- 2) Determining the relation (e.g., by multivariate linear regression) between small perturbations in the model parameters and resulting errors between the synthesized and the true image. The inverse of this relation can be used for adjusting model parameters such that the error will be minimized.
- 3) Establishing a procedure to apply the appearance model to an unknown image, and iteratively adjusting its model parameters to better match the image under investigation. The best match then renders the desired segmentation.

Together, these three aspects constitute an AAM segmentation method. In stage 1, the model generation, a set of training images with expert-drawn borders is analyzed.

All shapes in the set are described using point distribution models (PDM). All drawn shapes are represented as sets of  $N$  corresponding landmark points modeled as a  $2N$ -dimensional vector

$$\mathbf{x} = (x_1, y_1, x_2, y_2, \dots, x_N, y_N)^T. \quad (1)$$

All shape samples are aligned by Procrustes analysis [21] and an average shape  $\bar{\mathbf{x}}$  is calculated. By applying a PCA on the sample distribution, a set of shape eigenvectors is found that describes all significant shape variations over the training set in the order of their importance (corresponding eigenvalues). A subset of the eigenvectors describing a sufficient fraction of the total variation is grouped into a matrix  $\mathbf{P}_s$ . Each aligned sample  $\mathbf{x}$  within the distribution can now be approximated by the average shape with a linear combination of the eigenvectors superimposed

$$\mathbf{x} \approx \bar{\mathbf{x}} + \mathbf{P}_s \mathbf{b}_s \quad (2)$$

where  $\mathbf{b}_s$  is a vector containing the coefficients for each of the eigenvectors. This vector can be calculated by using the pseudoinverse of the matrix  $\mathbf{P}_s$  to find the projection of the shape on the space spanned by the eigenvectors

$$\mathbf{b}_s = \mathbf{P}_s^T (\mathbf{x} - \bar{\mathbf{x}}). \quad (3)$$

A similar approach is used to calculate a model of image appearance variations.

- 1) Warp all images so that their landmark points match the average shape. Subsampling with appropriate Gaussian filtering is applied here to limit the amount of data. Pixels inside an image patch spanned by the average shape are considered (i.e., the complete image near the shape, all pixels within the shape, plus a band of pixels surrounding the shape). The warping provides a shape-free image patch with the same number of pixels  $M$  for each example, which can be represented as a vector of intensities similar to (1)

$$\mathbf{g} = (g_1, g_2, \dots, g_M)^T. \quad (4)$$

- 2) Normalize intensity of each image patch and calculate the average normalized image  $\bar{\mathbf{g}}$ . In the original AAM implementation, this is done by linearly normalizing to the average intensity of the patch and a variance to best match the average normalized image. For ultrasound, we apply a nonlinear normalization before calculating the average image (see Section II-B).

- 3) Perform a PCA on the normalized intensity patches to get a matrix of eigenvectors  $\mathbf{P}_g$  that describes the principal intensity variations.
- 4) Express each intensity sample as a linear combination of eigenvectors similar to (2) and (3)

$$\mathbf{g} \approx \bar{\mathbf{g}} + \mathbf{P}_g \mathbf{b}_g \text{ and } \mathbf{b}_g = \mathbf{P}_g^T (\mathbf{g} - \bar{\mathbf{g}}).$$

- 5) Concatenate shape and intensity coefficient vectors:  $\mathbf{b} = (\mathbf{b}_s^T | \mathbf{b}_g^T)^T$  and perform another PCA to find a matrix of eigenvectors  $\mathbf{Q}$  describing simultaneous shape and intensity variations ("appearance"). Each example can now be expressed as a linear combination  $\mathbf{c}$  of these appearance eigenvariations:  $\mathbf{b} = \mathbf{Q}\mathbf{c}$ .

### B. Ultrasound-Specific Intensity Normalization

PCA models a multidimensional Gaussian distribution by calculating the centroid and main axes of the high-dimensional distribution ellipsoid. The intensity PCA, therefore, assumes a more or less Gaussian distribution of intensities over the set of samples for each element of the intensity vector (4) after intensity normalization. The standard AAM intensity normalization consists of a linear scale/offset correction for global lighting variations such that mean patch intensity is 0 and variance is 1. Such linear scale/offset intensity variations occur in echocardiograms as well, due to ultrasound gain/offset settings as well as video postprocessing. However, there is an extra complication. Echocardiograms have highly non-Gaussian intensity histograms. The image formation process described above (including speckle) gives it a somewhat "derivative" character, very different from typical real-world images. Histograms peak at very low intensities and tend to decrease exponentially. This is an intrinsic property of ultrasound images, more or less independent of the type of tissue and the scene involved. Consequently, the intensities in the image patches are not normally distributed; neither the distribution within individual patches nor the distributions of a certain patch point's intensities over the training set are Gaussian. In our findings, the patch histograms are roughly inversely exponential or chi-square distributed [Fig. 1(a)]. This chaotic plot (note the logarithmic scale) shows several noisy patch histograms, with widely varying skewness, range, and offsets.

Further video signal processing introduces more offset and gain variations, causing the histogram peak to shift considerably, and intensity ranges may differ greatly.

Therefore, we hypothesized that the standard linear intensity normalization and modeling with average and variance would not work well for ultrasound images. Because of the extremely skewed distributions, simple alignment to average and standard deviation of intensities will not produce the desired normalization. A special nonlinear intensity normalization was developed and employed, and AAMM results with and without this normalization were compared. The goal was to normalize the individual patch pixel's intensity distribution by calculating a global nonlinear intensity correction. If the intensities within a small region of one tissue class would be normally distributed (over the set of samples), then the joint distribution of many such regions would be more or less normally distributed as well. Since the overall joint distribution is not Gaussian or bimodal,

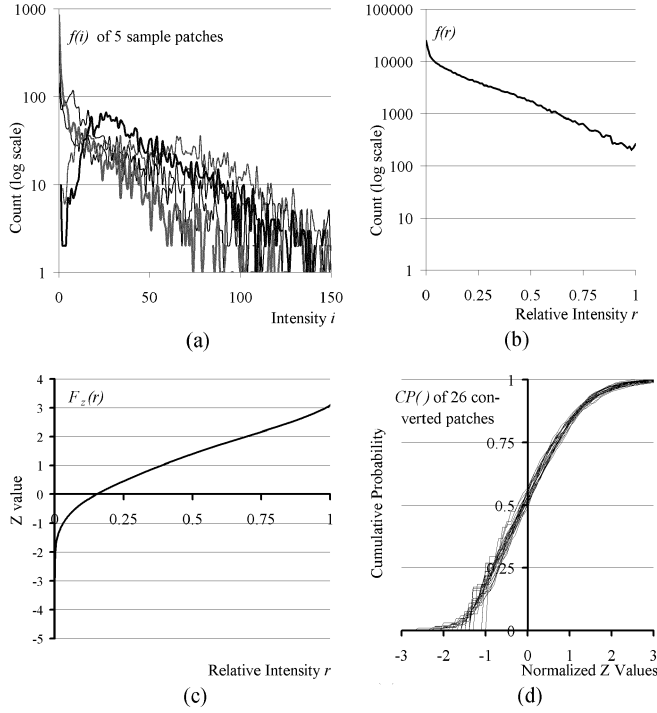


Fig. 1. Nonlinear normalization of intensities for echocardiographic image patches. (a) Uncorrected patch intensity histograms. (b) Total histogram of range-aligned distributions. (c)  $F_z(r)$  conversion function. (d) Normalized cumulative distributions.

we assume that the general shape of all regional distributions seriously contributes to the global distribution's shape. Transforming the overall distribution into a more or less normal distribution compensates for this effect as well as normalizes the regional distributions.

In the original AAM method, where Gaussian distributions are assumed, each image intensity vector  $\mathbf{g}_{im}$  is only scaled and offset, to minimize the effects of global lighting variation. All examples need to be best aligned to the normalized mean image  $\bar{\mathbf{g}}_z$ , which has an average of 0 and a variance of unity. For each example, a scaling  $\alpha$  and offset  $\beta$  are applied which are chosen to best match the intensity vector to the normalized mean. In the model creation step, the mean image is not yet established, but must be created from the normalized examples  $\mathbf{g}_z$ . This involves an iterative process

$$\begin{aligned} \mathbf{g}_z &= \frac{(\mathbf{g}_{im} - \beta \mathbf{I})}{\alpha} \\ \alpha &= \mathbf{g}_{im} \cdot \bar{\mathbf{g}}_z \\ \beta &= \frac{(\mathbf{g}_{im} \cdot \mathbf{I})}{n} \end{aligned} \quad (5)$$

where  $n$  is the number of elements in the vector,  $\mathbf{I}$  is the vector of all ones, and  $\bar{\mathbf{g}}_z$  is the mean of the normalized samples.

Before this normalization is applied, the following nonlinear normalization steps are performed to deal with the skewed and shifted intensity distributions. First, a linear range normalization realigns the upper and lower bounds of the distributions (rather than aligning their means). This is followed by a nonlinear intensity conversion that results in an approximately Gaussian distri-

bution. Converted intensities are further processed by the standard AAM normalization procedure.

- 1) For each patch  $\mathbf{g}_{im}$  individually, eliminate the range variability. Calculate the frequency distribution  $f(i)$  of the intensities  $i$  in  $\mathbf{g}_{im}$  and derive the cumulative probability density function  $CP_i(\cdot)$ . Due to the smoothing and warping, the intensities  $i$  are on a continuous scale rather than discrete. Thus, this involves numerical histogram integration (instead of summation), resulting in a fairly smooth function

$$\begin{aligned} CP_i(t) &= p(i \leq t) \\ &= \int_{-\infty}^t f(i) di / \int_{-\infty}^{\infty} f(i) di. \end{aligned} \quad (6)$$

Determine 0.1 percentile upper (up) and lower (lo) bounds of the intensity distribution

$$\begin{aligned} lo &= CP_i^{-1}(0.001) \\ up &= CP_i^{-1}(0.999). \end{aligned}$$

Transform all intensities  $i$  into range-normalized relative intensities  $r$  using  $r = (i - lo)/(up - lo)$  and clip between 0 and 1 to create the range-normalized intensity vector  $\mathbf{g}_r$ .

- 2) Calculate the total intensity distribution  $f(r)$  over the whole training set of range-normalized patches  $\mathbf{g}_r$  [Fig. 1(b)] and derive its cumulative probability density function  $CP_r(\cdot)$ .
- 3) The cumulative probability density function  $CP_Z(\cdot)$  of the standardized Gaussian distribution [ $Z$ , average 0, standard deviation (SD) of 1] is generally defined as

$$\begin{aligned} CP_Z(z) &= \frac{1}{2} \left( 1 - \operatorname{erf} \left( \frac{-z}{\sqrt{2}} \right) \right) \\ \operatorname{erf}(x) &= \frac{2}{\sqrt{\pi}} \int_0^x e^{-t^2} dt. \end{aligned} \quad (7)$$

Calculate a  $Z$ -value mapping function  $F_z(r)$  [Fig. 1(c)] that converts relative intensities  $r$  into the  $Z$  value that corresponds to the same cumulative probability

$$F_Z(r) = CP_Z^{-1}(CP_r(r)). \quad (8)$$

- 4) Use  $F_z(r)$  to transform all range-normalized patches  $\mathbf{g}_r$  in the training set to a  $Z$ -normalized  $\mathbf{g}_n$ .
- 5) Normalized patches  $\mathbf{g}_n$  are now processed by the standard AAM intensity normalization (5) where the average image is calculated iteratively. The cumulative distributions now closely match those of a normal distribution [Fig. 1(d)]. The mapping function  $F_z(r)$  is stored with the model.
- 6) During matching of a new image, step 1) is performed to get  $\mathbf{g}_r$ , step 4) is applied to get  $\mathbf{g}_n$ , and the standard AAM intensity normalization (5) is applied to get  $\mathbf{g}_z$ . Further processing is standard.

For each example, up, lo and  $\alpha$ ,  $\beta$  are calculated separately. The nonlinear mapping  $F_z(r)$ , however, is calculated once from the training set and is identical for all images. By aligning the bounds of the ranges before addition, the histogram shapes will match and a general histogram shape for the object under consideration will be found. Even though individual example objects may have differently shaped histograms, the function will have a normalizing effect and will reduce modeling problems.

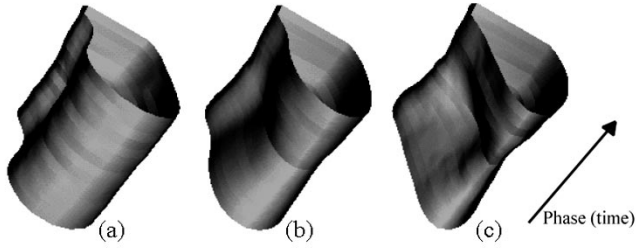


Fig. 2. Second eigenvariation of AAMM shape. The objects represent motion patterns; stacks of contours for the full cardiac cycle (time axis from bottom left to top right; the shape constriction in the middle corresponds to end-systole, the open ends to end-diastole). (a) Average shape motion pattern minus three standard deviations. (b) Average motion pattern. (c) Average plus three standard deviations.

### C. AAMM Generation

In the AAMM, the appearance of the heart is modeled for the entire cardiac cycle by considering the time sequence as a stack of 2-D images (time frames). All single-beat sequences are phase normalized into a fixed number of frames  $F$  so that end-diastolic and end-systolic frames map to the same frame number. The other frames are found by nearest neighbor interpolation. In the training set, corresponding shape points on the LV endocardial contour are defined for each time frame based on expert drawn contours. The sequence of contours is considered as a single shape sample (compare Fig. 2): the shape vectors for all time frames are concatenated in the order of their phase number and further treated as a single 2-D shape vector

$$\begin{aligned} \mathbf{x} &= (\underbrace{x_{11}, y_{11}, \dots, x_{1N}, y_{1N}}_{\text{Phase 1}}, \underbrace{x_{21}, y_{21}, \dots, x_{2N}, y_{2N}}_{\text{Phase 2}}, \\ &\quad \dots, \underbrace{x_{F1}, y_{F1}, \dots, x_{FN}, y_{FN}}_{\text{Phase } F})^T \\ &= (\mathbf{x}_1^T | \dots | \mathbf{x}_F^T)^T. \end{aligned} \quad (9)$$

Only the 2-D coordinates of the points are considered, so, unlike what Fig. 2 suggests, the third dimension is only implicitly involved.

The image appearance of the heart for each time frame is modeled as a vector of pixel intensity values in the shape-free image patch spanned by the corresponding average shape. The vectors of image patch intensities for each time frame are concatenated in the order of their phase number to a single intensity vector  $\mathbf{g} = (\mathbf{g}_1^T | \dots | \mathbf{g}_F^T)^T$ . The total intensity distributions are normalized nonlinearly as described above. The length of the resulting shape and intensity vectors is approximately  $F$  times larger than in a corresponding 2-D AAM (note that different phases do not need to have the same number of landmarks or pixels).

PCA on the set of training time sequences renders the mean and eigenvariations of shape and motion (Fig. 2) and intensity appearance (the “average heartbeat,” Fig. 3) over the complete cardiac cycle.

### D. Matching the AAMM to Image Sequences

The AAMM is applied to segmentation of a phase-normalized image sequence by minimizing the difference between the synthesized model appearance and the whole target time stack

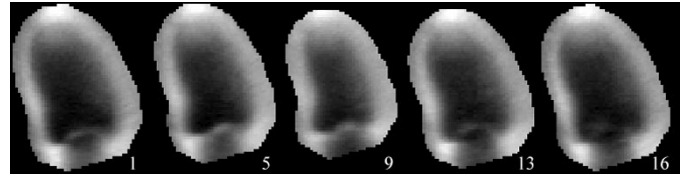


Fig. 3. “Average heartbeat” of the LV in four-chamber view over 65 patients, five of 16 cardiac phases shown. Left to right: (1) End-diastole. (5) Mid-systole. (9) End-systole. (13) Mid-diastole. (16) Atrial filling.

by varying the pose and deforming the appearance motion model along the characteristic model eigenvariations using a gradient descent minimization. This involves finding an affine transformation, global intensity parameters, up, lo,  $\alpha$ ,  $\beta$ , and appearance coefficients that minimize the root-mean-square (rms) difference between the synthetic appearance model sequence and the target image sequence. This procedure results in a time-continuous segmentation for the complete cardiac cycle.

The AAMM matching procedure resembles conventional 2-D AAM matching. However, the rms error criterion and the parameter regression matrices for the appearance coefficients, pose, and global intensity are calculated for the full image sequences in AAMMs, as opposed to a single 2-D image frame in AAMs. Therefore, the temporal coherence in the cardiac motion is preserved during the matching, ensuring a segmentation result which is largely consistent with the cardiac motion patterns observed in the training set.

Apart from the nonlinear intensity normalization described in Section II-B, ultrasound-specific parts of the matching method include the initialization of pose (translation, scale, and rotation) to averages found from the training set. As the field of view of an ultrasound probe is quite limited, the actual variations in position, orientation, and size are relatively small. Therefore, an initialization to the average pose in the training set renders good results and eliminates the need for multiple initializations or manual positioning of the model.

## III. EXPERIMENTS

### A. Data

Echocardiographic transthoracic four-chamber sequences were acquired from 129 unselected infarct patients participating in a clinical trial. No patients were excluded for reasons of image quality. Images were digitized from videotape at a resolution of  $768 \times 576$  pixels with different calibration factors (0.28 to 0.47 mm/pixel). End-diastolic and end-systolic frames were marked by the expert observer. All single-beat sequences were phase normalized to  $F = 16$  frames so that end-diastolic (ED) and end-systolic (ES) frames mapped to the same frame number (1, 9, and 16, respectively).

### B. Independent Standard, Training, and Analysis

In all sequences, an expert observer who was blind to the computer analysis results outlined the contours of the LV endocardium in all frames of the image sequences. This was done manually for ED and ES; for the remaining images, a semi-automated detection was used based on these ED/ES borders

TABLE I  
AAMM RESULTS ON TEST SET AND COMPARISON TO TRAINING SET AND MANUAL INTER/INTRAOBSERVER RESULTS

Results (mean $\pm$ SD)	Test set (n = 62 of 64)	Training set (n = 61 of 65)	Manual Intraobserver	Manual Interobserver
Success score (%)	96.9% (62/64)	93.8% (61/65)	-	-
Point distance (mm)	$3.35 \pm 1.22$	$0.12 \pm 0.36 \dagger$	$2.32 \pm 0.75 \dagger$	$3.82 \pm 1.44 \dagger$
Fractional area error (%)	$-2.89 \pm 10.2$	$0.07 \pm 1.08 * \dagger$	$0.92 \pm 6.19 \dagger$	$-4.39 \pm 10.3$
Ejection Fraction error (%)	$0.66 \pm 5.5 *$	$-0.05 \pm 0.41 *$	$-1.71 \pm 2.84$	$0.88 \pm 3.15 *$
Area regression (cm <sup>2</sup> )	$y = 0.91x + 1.73$	$y = 1.00x + 0.001$	$y = 0.87x + 3.57$	$y = 0.95x + 0.15$
(y=computer, x>manual)	$r = 0.87$	$r = 0.999$	$r = 0.96$	$r = 0.88$

\* : mean not significantly different from 0;  $\dagger$  : mean significantly larger/smaller than mean of test set

(ECHO-CMS system [1]). In all cases, manual corrections were applied until the expert was completely satisfied with all resulting borders. The expert-validated contour set was, therefore, considered equivalent to a manually defined set. In total, 2064 ultrasound frames were available with an accompanying independent standard. The total data set was split randomly into a training set of 65 patients and a testing set of 64 patients. Each contour was modeled by 37 landmark points, of which the apex and mitral valve attachments were true anatomic landmarks; the other points were defined by regular subdivision of the manually defined contours. The AAMM created from the training set was applied to segmentation of the 64 sequences forming the testing set. All models were initialized to the same fixed initial pose, which was the average pose obtained from the training set. For comparison, matching was also performed on the training set.

#### C. Intra- and Interobserver Variability of Independent Standard

To determine the reliability of the independent standard, a limited inter- and intraobserver variability study was performed. For 20 randomly selected patients, contours were drawn independently by a second observer, and for a second time (with an interval of six months) by the first observer. Differences in areas and unsigned point distances were determined as described below for the manual/computer comparisons.

#### D. Quantitative Validation

Five quantitative indices were calculated per patient to compare the automatically detected contours with the observer-identified independent standard. Endocardial border positioning error was defined as the average of all 592 unsigned distances between corresponding contour points over the full cycle. Note that these are Euclidean distances between corresponding landmarks, not minimal distances of points to contours. The latter give lower errors but tend to obscure matching errors along the border, missed end points, etc. The success rate of the automated matching was determined as the number of patients with endocardial border positioning error below a predefined threshold. Endocardial percent area errors were determined separately for each phase of the cardiac cycle, where endocardial area was defined as area enclosed by the endocardial border. The area ejection fraction was determined as  $(1 - (\text{Area}_{\text{ES}}/\text{Area}_{\text{ED}}))$ ; the area ejection fraction error was the difference between the computer-determined and manually defined ejection fraction. All mean errors were tested against the mean errors of the test set and against zero. Statistical significance was determined with

a one-sided  $t$  test, where  $p < 0.01$  was considered significant. Linear area regressions were also performed.

#### E. Validation of Nonlinear Intensity Normalization

To determine the contribution of the ultrasound-specific nonlinear normalization of intensities, the total evaluation was repeated without this normalization in model generation, regression training, and matching. The standard AAM normalization as described by (5) was used instead. All other parameters were identical. The same quantitative indices as described above were calculated.

#### F. Comparison of AAMM With Multiple AAMs

We hypothesized that AAMMs could better exploit the temporal continuity of the image data than AAMs. To test this hypothesis, we compared the results of the 16-phase AAMM with the combined results of 16 single-phase AAMs, each trained and tested on images of only one phase, with all other parameters identical. Average and standard deviation of endocardial border positioning errors for the 16-phase AAMM were compared to the pooled average and standard deviation of the set of single-phase AAMs. The AAMM average error was tested for being significantly lower using a single-sided  $Z$  test. Percent area errors were compared between each single-phase AAM and the corresponding phase of the 16-phase AAMM.

## IV. RESULTS

#### A. Inter- and Intraobserver Variability

From the 20 randomly chosen patients, one patient with an extremely dilated ventricle of  $>250$  ml posed problems in interpretation and constituted an extreme outlier in the comparisons. This patient was excluded and results over the 19 remaining patients are listed in Table I. As expected, intraobserver variabilities are generally smaller than interobserver variabilities. The criterion for a successful match in further experiments was derived from the found point distances in the interobserver variability ( $3.82 \pm 1.44$  mm): an average point distance  $< 8$  mm (equivalent to interobserver mean  $+3$  SD) was considered successful, as it lies within the bounds of human variability. This criterion is mainly a test to remove apparent convergence failures from further statistical analysis. For claiming clinical success, a narrower criterion could be chosen; several are listed next.

Inter- and intraobserver variabilities of manual contours as found in this study were comparable to those reported in

TABLE II  
AAMM RESULTS WITH NONLINEAR AND LINEAR INTENSITY NORMALIZATION

Results (mean $\pm$ SD)	Nonlinear intensity normalization		Standard linear normalization	
	Test set (n = 64)	Training set (n = 65)	Test set (n = 64)	Training set (n = 65)
Success score (success/total)	96.9% (62/64)	93.8% (61/65)	73.4% (47/64)	80% (52/65)
Point distance (mm)	$3.54 \pm 1.62$	$0.75 \pm 2.53$ †	$5.73 \pm 3.01$ †	$3.75 \pm 4.35$ †
Fractional area error (%)	$-3.70 \pm 11.0$	$-1.84 \pm 8.22$ †	$-5.72 \pm 16.18$ †	$-6.15 \pm 14.1$ †
Ejection Fraction error (%)	$0.99 \pm 5.7$ *	$0.43 \pm 2.68$ *	$1.04 \pm 6.77$ *	$1.07 \pm 4.86$ *
Area regression (cm <sup>2</sup> )	$y = 0.77x + 5.51$	$y = 0.88x + 2.77$	$y = 0.79x + 4.25$	$y = 0.83x + 2.90$
(y=computer, x=manual)	$r = 0.84$	$r = 0.89$	$r = 0.76$	$r = 0.76$

\* : mean not significantly different from 0; † : mean significantly larger/smaller than mean of test set (nonlinear normalization)

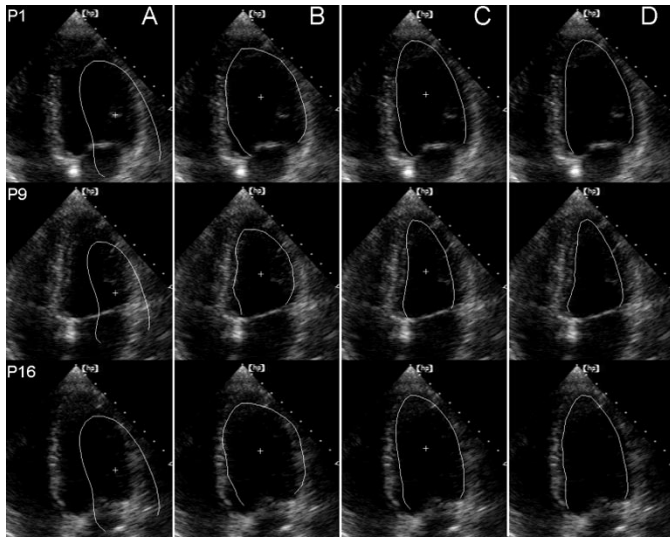


Fig. 4. Example result of fully automated AAMM segmentation of an echocardiographic image sequence from the test set, spanning over one heartbeat. Segmentation was performed simultaneously in all 16 image phases. From top to bottom, partial images from phase 1, 9, and 16 are shown. (a) Initial 16-phase AAMM model positioned on phase images 1, 9, and 16. (b) AAMM match after five iterations. (c) Final match after 20 AAMM iterations. (d) Observer-identified endocardial contours shown for comparison.

other studies, although direct comparisons are difficult due to dependence on the measurement protocol, number and type of patients, and image quality. For example, Gordon *et al.* [22] report the SD of interobserver percental error in LV area-length volumes: 8.5% for ED, 16.5% for ES, comparable to the SD of interobserver percental error in LV area of 10.3% (all phases) in our study.

### B. Test Set

An example of the matching process is given in Fig. 4(a)–(c). The corresponding contours manually defined by an independent expert are shown for comparison in Fig. 4(d).

In 62 of all 64 tested patients (97%), the AAMM converged successfully (average point distance  $< 8$  mm). To give a better impression of the range of positioning errors in relation to the interobserver error, the percentage of patients with average point distance  $< 3.82$  mm (the interobserver mean variability) was 72%;  $< 5.26$  mm (mean + 1 SD): 89%;  $< 6.7$  mm (mean + 2 SD): 94%. The two cases where the matching failed (distances of 9.2 and 9.9 mm) were excluded from further statistical analysis. In

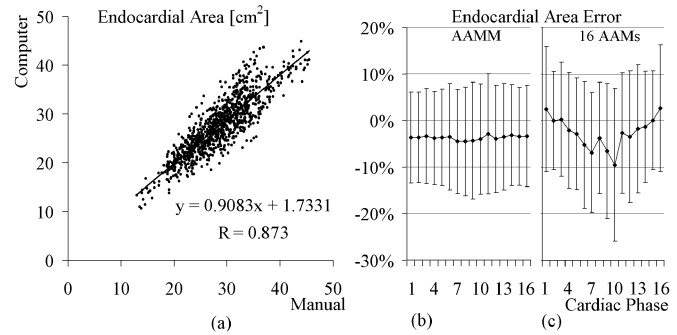


Fig. 5. Validation results. (a) Comparison of the observer-defined and computer-determined LV endocardial areas in the 992 test set images from 62 out of 64 patients. The regression analysis compared areas detected in all 16 cardiac phases. (b) Endocardial percent area error as a function of cardiac phase. Mean error  $\pm$  SD is shown. (c) Endocardial percent area error for 16 single-phase AAMs.

the 62 successful matches, the fully automatically found borders agreed well with the independent standard (Table I) with mean unsigned border positioning errors of  $3.35 \pm 1.22$  mm ( $9.3 \pm 3.2$  pixels). Results for the full set of 64 tested subjects can be found in Table II. Fig. 5(a) demonstrates a very good correlation of the observer-identified and AAMM-determined LV endocardial areas ( $r = 0.87$ ). Endocardial percent area error averaged over all phases was  $-2.89 \pm 10.2\%$ , showing a slight but significant negative bias of the AAMM areas. Mean signed and unsigned area ejection fraction errors were small:  $0.66 \pm 5.5\%$  and  $4.6 \pm 3.0\%$ , respectively. Variability in ejection fraction was too high to reach significance in the relatively few measurements. Fig. 5(b) shows the endocardial percent area error as a function of cardiac phase, demonstrating that the border detection accuracy does not change substantially along the cardiac cycle. Comparison with the inter- and intraobserver variabilities clearly shows that the fully automated AAMM detection performed significantly better or at least equivalent to interobserver variabilities. In other words, the AAMM generally performs better than a second independent observer. A repetition by the first observer would generally be significantly superior to the AAMM result on an unseen (test) patient. However, the intraobserver variability can be seen as a measure for inaccuracies in the training data set that was used to generate the AAMM. Such inconsistencies are likely to limit the overall accuracy of the AAMM. The intraobserver errors are, therefore, a plausible lower bound of the AAMM accuracy.

### C. Training Set

For comparison, matching was performed on the training set as well. Here, four of 65 patients showed a failed match (distances 9.3–12.5 mm). For all others, the match was nearly perfect on all results (Table I). All failed matches could be attributed to the model's initialization to the average pose of the set; as expected, a manual re-initialization closer to the true pose gave a near-perfect result in each case. These results confirm the correctness of the implemented methods.

### D. Nonlinear Intensity Normalization

The nonlinear intensity normalization causes a dramatic improvement in match results (Table II). When it is left out, the test-set failure rate increases from 3% to 27%. In order to make a fair comparison, all results were compared over the full set without eliminating failures.

The nonlinear normalization renders significantly better results for all measures, both for the training set and the test set (area ejection fraction error improvement is not insignificant). The obvious matching improvement in the training set (where the model in principle can match each example closely) shows that a major disturbing factor in the method has been eliminated. These results confirm our hypothesis that the non-Gaussian distribution of the ultrasound intensities is not handled well by the standard intensity normalization, and it proves that the correction is successful.

### E. AAMM Versus AAM

The pooled average border positioning error for the set of 16 single-frame AAMs was  $4.27 \pm 2.52$  mm ( $n = 1024$ ,  $16 \times 64$  frames in test set) whereas for the 16-frame AAMM, it was  $3.54 \pm 1.62$  mm. This 17% improvement is highly significant ( $p \ll 0.001$ ). The percent endocardial area errors in Fig. 5(b) and (c) shows that the AAMM [Fig. 5(b)] does indeed show a much more consistent behavior over the phases, with generally 15% lower standard deviation.

## V. DISCUSSION

We found that the AAMM method performed very well in clinical quality ultrasound images. The specific nonlinear intensity normalization contributes substantially to this.

The AAMM approach is a highly general extension of standard AAM and is applicable in any multidimensional case where a fixed image indexing (in time or space) is appropriate.

The appearance motion model captures typical motion patterns associated with cardiac contraction. An example is given in Fig. 2, where it is shown that a dilation of the apex is typically associated with a reduced displacement at end-systole (hypokinesis). Our hypothesis that an AAMM can better exploit temporal consistency in the data was confirmed by the highly significant 17% border error improvement reported in Section IV-E.

### A. Comparison to Other AAM Approaches

The limitation to a fixed number of slices distinguishes the AAMM approach from a real 3-D AAM. However, in the anisotropic 2-D+time case, a real 3-D AAM (employing

3-D coordinates, and allowing for 3-D rotations, translations, and scaling) would be less appropriate, as free 3-D rotation is meaningless in that case. Furthermore, a full 3-D AAM implementation has not been reported yet.

On the other hand, the phase normalization poses a practical limitation. The cardiac phase must be known beforehand, and borders are only found for the 16 frames. If contours for other frames are needed as well, an additional step is required. As we already have a close approximation of this border, numerous techniques can be used for this.

The coupled-view AAMs recently introduced by Cootes *et al.* [23] may provide similar facilities. In this approach, separate models are trained for different related “views,” of which the interdependencies are incorporated by applying another PCA over the parameters. Provided that linearity applies and no significant variability is eliminated during model generation, this may render similar results as an AAMM. However, this was not further investigated.

### B. Comparison to Other Echocardiographic Segmentation Techniques

In comparison to some other proposed techniques for spatiotemporal segmentation of echocardiograms, the AAMM approach has several clear advantages. In most approaches (e.g., by Montagnat *et al.* [14] and Angelini *et al.* [15]), the cardiac shape models are simple and not restricted to anatomically probable shapes. Endocardial points are localized from gradient-based features, which is problematic in regions with weak gradients and in cases where an expert would choose a different position. Jacob *et al.* [16] uses a simple PCA-based description of shape, but temporal behavior is modeled with a Kalman filter prediction of shape change over time. In AAMM, we use PCA modeling for both the temporal and spatial shape patterns. We do not employ a sophisticated noise suppression and feature extraction, but the high spatial frequencies and effects of more random nature are suppressed in the model by the spatial averaging and the PCA analysis. Jacob's approach is similar to an ASM, as it is based on finding candidate gradient-based edge points along profiles near the estimated border. An AAM approach like ours is based on image intensity patterns over the whole object of interest and does not rely on strong edge features to localize positions.

It is hard to compare our results directly to other automated border detection results, since the circumstances under which such results are attained can be totally different. We found no other studies doing a similar fully automated analysis on large numbers of unselected patients, clinical image quality, etc. Therefore, comparison to the corresponding human interobserver variability on the same data set (as reported above) is appropriate.

### C. Landmark Definitions and Shape Correspondence

Another issue of interest is the definition of point correspondence between training shapes. This is an actively researched field both in 2-D and 3-D [24]–[26], where correspondence is established based on shape features. The AAMM approach applies a straightforward shape modeling and analysis, identical to that described by Cootes *et al.* In our application, the



sampling of training shapes to certify point correspondence between examples is based on three expert-defined anatomical landmarks and an equidistant contour subsampling in between. For our purpose (endocardial border detection), we employ relatively smooth borders and the distribution of the intermediate points over the border is of little interest. If more detailed shapes or landmark displacements along the contour are desired, a more elaborate shape alignment and point sampling would be required during the training phase. In that case, automated anatomical landmark placement should probably be based on image features rather than shape analysis, as proposed by Walker *et al.* [27].

#### D. Results, Limitations and Further Improvements

The results of the presented ultrasound case studies showed a high robustness (97% successful matches) of our fully automated AAMM approach. The fully automatically detected contours demonstrated good accuracy, both in border positioning errors and in endocardial area measures. The errors compare favorably to the found inter- and intraobserver variabilities associated with manual tracing and, therefore, are clinically acceptable. The detected contours were highly similar to the manually defined contours in the sense that papillary muscles, trabecular structures, and apical noise were successfully excluded from the contours. The AAMM method, however, has a tendency to prefer a "too-normal" contraction pattern. This can be seen from the regression lines: Extreme values seem to be harder to find. This may be caused by the optimization process getting trapped in local minima. In other model-based techniques such as snakes, a direct balance between an internal (model) and external (image) force is established, and the local strength of model and image features may cause problems. This is less of a problem in AAMs, where the driving force is the residual image difference between synthetic and real image, the content of which determines the size and direction of the update step in the parameter space. Variations in the gradient descent optimization method, multiple initializations, a multiresolution approach [18], hybrid AAM/ASM approach [19], or modeling other structures like epicardium, right ventricle, and valves may help to surpass local minima. Match results on the training data confirm that model initialization and/or lock-in range are candidates for improvement. Alternatively, if a very localized and precise detection is required, a combination with a local contour optimization (dynamic programming [1], snakes [10]) may be attempted.

For a practical application, we strive toward minimal user interaction to attain maximal automation and limit sources of variability. However, the user should always be allowed to apply additional corrections. AAMs allow a very elegant approach for interactive corrections, as recently described by Cootes and Taylor [28].

The described approach is not free of some limitations. As any AAM approach, its reliability depends on the range of variabilities covered in the training set. In case of clinical images, the patient set should include sufficient cases of expected pathologies. Also, images from different types of equipment or special imaging modes (use of contrast, harmonic imaging, etc.) may influence accuracy and may require training of specialized

models. This is a topic of further investigation. Furthermore, the result is clearly limited by the quality and reproducibility of the training image and contour data: accurately validated borders on substantial data sets are required.

The temporal segmentation approach is fully automated for phase-normalized sequences, not requiring any operator interaction. Indicating the ED and ES frames for phase normalization, however, was not done automatically in this study, although ED images can be easily identified automatically using the ECG. It remains to be investigated whether good results can be achieved as well for sequences normalized on the ED frames only.

Segmentation of a 16-phase image sequence is fast with typical processing times of 6 s on an 800-MHz Windows PC. To our knowledge, no other fully automated approach has been reported yielding comparable results in a large clinical evaluation. Still, additional development is needed to include all standard views, all representative pathologies and determine the routine clinical performance in a large scale clinical study validation.

In this study we have shown that AAMMs can automatically detect endocardial contours practically equivalent to those defined by a human expert. We should note that the clinical quality of quantitative information derived from these contours remains to be determined. We expect the AAMM method to be useful for full-cycle LV volume measurements, locating and quantifying wall motion abnormalities, localizing ischemia, etc. Proving its clinical significance for such applications is beyond the scope of this paper and remains the subject of future clinical studies.

## VI. CONCLUSION

An AAM for normalized time sequences (AAMM) has been developed that models time-continuous cardiac motion and image appearance and performs fast, robust, fully automated contour detection on phase-normalized cardiac time sequences in a practically applicable manner. It generates time-continuous segmentation results, which are consistent with cardiac dynamics. The AAMM demonstrated robustness and accuracy in a large clinical study of LV segmentation using four-chamber transthoracic ultrasound image sequences.

## REFERENCES

- [1] J. G. Bosch, G. van Burken, F. Nijland, and J. H. C. Reiber, "Overview of automated quantitation techniques in 2-D echocardiography," in *What's New in Cardiovascular Imaging*, J. H. C. Reiber and E. E. van der Wall, Eds. Dordrecht, The Netherlands: Kluwer, 1998, pp. 363–376.
- [2] D. B. Sher, S. Revankar, and S. Rosenthal, "Computer methods in quantitation of cardiac wall parameters from two-dimensional echocardiograms: A survey," *Int. J. Cardiac Imaging*, vol. 8, pp. 11–26, 1992.
- [3] J. E. Perez, A. D. Waggoner, B. Barzilai, H. E. Melton, J. G. Miller, and B. E. Sobel, "On-line assessment of ventricular function by automatic boundary detection and ultrasonic backscatter imaging," *J. Amer. College Cardiol.*, vol. 19, pp. 313–320, 1992.
- [4] E. A. Geiser, D. C. Wilson, D. X. Wang, D. A. Conetta, J. D. Murphy, and A. D. Hutson, "Autonomous epicardial and endocardial boundary detection in echocardiographic short-axis images," *J. Amer. Soc. Echocardiogr.*, vol. 11, pp. 338–348, 1998.
- [5] T. Brotherton, T. Pollard, P. Simpson, and A. DeMaria, "Echocardiogram structure and tissue classification using hierarchical fuzzy neural networks," in *Proc. IEEE Conf. Acoustics, Speech and Signal Processing*, vol. 2, Adelaide, SA, Australia, Apr. 1994, pp. 573–576.
- [6] J. M. B. Dias and J. M. N. Leita, "Wall position and thickness estimation from sequences of echocardiographic images," *IEEE Trans. Med. Imag.*, vol. 15, pp. 25–38, Feb. 1996.

- [7] T. Gustavsson, S. Molander, R. Pascher, Q. Liang, H. Broman, and K. Caidahl, "A model-based procedure for fully automated boundary detection and 3-D reconstruction from 2-D echocardiograms," in *Proc. Computers in Cardiology*, Bethesda, MD, Sept. 1994, pp. 209–212.
- [8] N. Friedland and D. Adam, "Echocardiographic myocardial edge detection using an optimization protocol," in *Proc. Computers in Cardiology*, Jerusalem, Israel, Sept. 1989, pp. 379–382.
- [9] M. Belohlavek, A. Manduca, T. Behrenbeck, J. Seward, and J. F. Greenleaf, "Image analysis using modified self-organizing maps: Automated delineation of the left ventricular cavity in serial echocardiograms," in *Proc. Visualization in Biomedical Computing Conf.*, Hamburg, Germany, Sept. 1996, pp. 247–252.
- [10] V. Chalana, D. T. Linker, D. R. Haynor, and Y. Kim, "A multiple active contour model for cardiac boundary detection on echocardiographic sequences," *IEEE Trans. Med. Imag.*, vol. 15, pp. 290–298, June 1996.
- [11] T. Hozumi *et al.*, "Echocardiographic estimation of left ventricular cavity area with a newly developed automated contour tracking method," *J. Amer. Soc. Echocardiogr.*, vol. 10, pp. 822–829, 1997.
- [12] A. D. Parker, A. Hill, C. J. Taylor, T. F. Cootes, X. Y. Jin, and D. G. Gibson, "Application of point distribution models to the automated analysis of echocardiograms," in *Proc. Computers in Cardiology*, Bethesda, MD, Sept. 1994, pp. 25–28.
- [13] T. F. Cootes, A. Hill, C. J. Taylor, and J. Haslam, "Use of active shape models for locating structures in medical images," *Image Vision Comput.*, vol. 12, pp. 355–366, 1994.
- [14] J. Montagnat, H. Delingette, and G. Malandain, "Cylindrical echocardiographic image segmentation based on 3-D deformable models," in *Proc. Conf. Medical Image Computing and Computer Aided Intervention (MICCAI'99)* Cambridge, U.K., 1999, pp. 168–175.
- [15] E. D. Angelini, A. F. Laine, S. Takuma, J. W. Holmes, and S. Homma, "LV volume quantification via spatiotemporal analysis of real-time 3-D echocardiography," *IEEE Trans. Med. Imag.*, vol. 20, pp. 457–469, June 2001.
- [16] G. Jacob, J. A. Noble, M. Mulet-Parada, and A. Blake, "Evaluating a robust contour tracker on echocardiographic sequences," *Med. Image Anal.*, vol. 3, pp. 63–75, 1999.
- [17] T. F. Cootes, G. J. Edwards, and C. J. Taylor, "Active appearance models," *IEEE Trans. Pattern Anal. Machine Intell.*, vol. 23, pp. 681–685, June 2001.
- [18] T. F. Cootes and C. J. Taylor, "Statistical models of appearance for medical image analysis and computer vision," in *Proc. SPIE Medical Imaging 2001* San Diego, CA, 2001, pp. 236–248.
- [19] S. C. Mitchell, B. P. F. Lelieveldt, R. J. van der Geest, H. G. Bosch, J. H. C. Reiber, and M. Sonka, "Multistage hybrid active appearance model matching: Segmentation of left and right ventricles in cardiac MR images," *IEEE Trans. Med. Imag.*, vol. 20, pp. 415–423, May 2001.
- [20] H. G. Bosch, S. C. Mitchell, B. P. F. Lelieveldt, M. Sonka, F. Nijland, and J. H. C. Reiber, "Feasibility of fully automated border detection on stress echocardiograms by active appearance models," *Circulation*, vol. 102, p. II-633, abstract, 2000.
- [21] C. Goodall, "Procrustes methods in the statistical analysis of shape," *J. Royal Stat. Soc. B*, vol. 53, pp. 285–339, 1991.
- [22] E. P. Gordon, I. Schnittger, P. J. Fitzgerald, P. Williams, and R. L. Popp, "Reproducibility of left ventricular volumes by two-dimensional echocardiography," *J. Amer. College Cardiol.*, vol. 2, pp. 506–513, 1983.
- [23] T. F. Cootes, G. V. Wheeler, K. N. Walker, and C. J. Taylor, "Coupled-view active appearance models," in *Proc. British Machine Vision Conf.*, vol. 1, Bristol, U.K., Sept. 2000, pp. 52–61.
- [24] H. D. Tagare, "Shape-based nonrigid correspondence with application to heart motion analysis," *IEEE Trans. Med. Imag.*, vol. 18, pp. 570–579, July 1999.
- [25] A. F. Frangi, D. Rueckert, J. A. Schnabel, and W. J. Niessen, "Automatic 3-D ASM construction via atlas-based landmarking and volumetric elastic registration," in *Proc. Conf. Information Processing in Medical Imaging*, Davis, CA, June 2001, pp. 78–91.
- [26] R. H. Davies, T. F. Cootes, and C. J. Taylor, "A minimum description length approach to statistical shape modeling," in *Proc. Conf. Information Processing in Medical Imaging*, Davis, CA, June 2001, pp. 50–63.
- [27] K. N. Walker, T. F. Cootes, and C. J. Taylor, "Automatically building appearance models from image sequences using salient features," in *Proc. British Machine Vision Conf.*, Nottingham, U.K., Sept. 1999, pp. 463–472.
- [28] T. F. Cootes and C. J. Taylor, "Constrained active appearance models," in *Proc. IEEE Int. Conf. Computer Vision*, vol. 1, Vancouver, BC, Canada, 2001, pp. 748–754.